Preparation of carbon nitride nanotubes with P-doping and their photocatalytic properties for hydrogen evolution

Dawoon Jang [a,1], Suyeon Lee [a,1], Nam Hee Kwon [b,1], Taehoon Kim [b], Sangjoon Park [a], Kyung Yeon Jang [c], Eojin Yoon [c], Seungjoo Choi [a], Juheon Han [a], Tae-Woo Lee [c,d], Jeongho Kim [a], Seong-Ju Hwang [b,**], Sungjin Park [a,*]

[a] Department of Chemistry and Chemical Engineering, Inha University, 100 Inha-ro, Michuhol-gu, Incheon, 22212, Republic of Korea
[b] Department of Materials Science and Engineering, College of Engineering, Yonsei University, 50 Yonsei-ro, Seodaemun-gu, Seoul, 03722, Republic of Korea
[c] Department of Materials Science and Engineering, Seoul National University, 1 Gwanak-ro, Gwanak-gu, Seoul, 08826, Republic of Korea
[d] School of Chemical and Biological Engineering, Institute of Engineering Research, Research Institute of Advanced Materials, Soft Foundry, Seoul National University, 1 Gwanak-ro, Gwanak-gu, Seoul, 08826, Republic of Korea

ARTICLE INFO

ABSTRACT

Various carbon nitride (C_3N_4) materials show great potential as an eco-friendly, visible-light-active photocatalyst for hydrogen evolution reaction (HER). In this work, a new route to produce one-dimensional (1D) P-doped carbon nitride nanotubes is developed via supramolecular self-assembly. The nanotubes are produced by thermal condensation of melamine and cyanuric acid. The addition of an ionic liquid (1-butyl-3-methylimidazolium hexafluorophosphate) improves the uniformity of the nanotubes. It is revealed that the C_3N_4 nanotubes are formed by thermal condensation of rod-shaped intermediates. The nanotubes show an excellent photocatalytic HER activity under visible light irradiation and are a superior catalyst to 3D C_3N_4 samples. From thorough structural and photophysical characterizations, it is found that the nanotubes contain larger surface areas, more amine bridges, better crystallinity, and more visible-light-absorption ability than control samples. These structural features are reasons for the enhanced photocatalytic performance.

Carbon nitride refers to various binary materials containing C and N atoms linked by covalent bonds and the most stable form is C_3N_4 [1–3]. This three-dimensional (3D) solid material, which consists of layers of 2D C_3N_4 and is produced by the polycondensation of small organic molecules, is typically referred to as polymeric or graphitic C_3N_4 (p- or g-C_3N_4) [4,5]. Tri-*s*-triazine rings containing alternating C and N structures with sp^2 hybridization are a basic building unit of the material and are linked through tertiary amine bridges [6–8].

Recently, 3D C_3N_4 materials have been studied as visible-light-active photocatalysts due to their suitable electronic structure for absorbing visible light [9–11]. In particular, they show excellent photocatalytic properties for the hydrogen evolution reaction (HER) [12,13], the reduction of CO_2 [14], and the degradation of organic pollutants [15], which are all important for solving energy and environmental issues. Although various metal-containing semiconductors exhibit promising photocatalytic behavior, 3D C_3N_4 materials have been explored as

metal-free and eco-friendly photocatalysts.

The photocatalytic properties of C_3N_4 materials can be improved by increasing their surface area and modulating their electronic structure. Porous 3D or exfoliated 2D C_3N_4-based materials have been successfully used in the preparation of efficient photocatalysts with high surface area and improved visible light absorption ability [16]. Additionally, 1D nanotubular C_3N_4 structures are intriguing platforms for photocatalysis owing to their possible access to photocatalytic active species at both their internal and external surfaces and facile transfer of photogenerated charge carriers with low resistance. Recent attempts have generated efficient C_3N_4 nanotube photocatalysts for the HER and the degradation of organic pollutants [17,18]. However, it is still necessary to develop eco-friendly methods without the use of hard templates and toxic chemicals and to understand the effect of 1D structures on the enhancement of photocatalytic performance.

Heteroatom doping into the C_3N_4 network is a common method for

* Corresponding author.
** Corresponding author.
  E-mail addresses: hwangsju@yonsei.ac.kr (S.-J. Hwang), sungjinpark@inha.ac.kr (S. Park).
[1] These authors contributed equally.

controlling electronic structures such as energy levels of conduction, valence band edges, and mid-gap state [19–21]. While B, S, and P have all been used as dopants, it is suggested that P-doping strongly affects electrical and thermal conductivity because it enhances charge carrier mobility.

Various C- and N-containing molecules such as melamine, dicyandiamide, and urea have been used as precursors to produce 3D C_3N_4 [22]. Self-assembly between the precursor and other molecules through H bonding is a promising route for controlling shape and morphological properties [13,23]. Herein, we developed a new route to produce 1D C_3N_4 nanotubes *via* the supramolecular self-assembly of melamine and cyanuric acid. The use of an ionic liquid (1-butyl-3-methylimidazolium hexafluorophosphate, $BmimPF_6$) improves the uniformity of the tube materials. The resulting C_3N_4 nanotubes showed significantly improved photocatalytic HER activity under visible-light irradiation. Various control samples were prepared to understand the formation mechanism of tube materials. The chemical structure and photophysical properties of the tube materials were intensively studied with various characterization techniques, including solid-state nuclear magnetic resonance (SSNMR), 2D excitation-emission mapping (2D EEM), and time-resolved photoluminescence (TR-PL) spectroscopy. Furthermore, their relationship with photocatalytic HER activity was elucidated.

1. Experimental section

1.1. Preparation of M-CN

Melamine (5 g, Aldrich, 99%) was loaded into a quartz crucible and placed in the center of a tube furnace, followed by several cycles of vacuum degassing and filling with N_2. The tube furnace was heated to 550 °C at a rate of 10 °C/min and held for 4 h under an N_2 gas flow. After cooling to room temperature, the resulting product was obtained as a yellow powder. The powder (200 mg) was sonicated with an HCl solution (1 M, 150 mL) for 200 min in a round-bottom flask to remove the remaining impurities. It was then filtered using a membrane filter (Advantech Corp., Model: H020A047A) and washed with deionized water several times. Drying under vacuum for 12 h at room temperature afforded the final product, denoted as M-CN.

1.2. Preparation of MCP-CN

Melamine (2.5 g, Aldrich, 99%) and cyanuric acid (2.5 g, Aldrich, 98%) were dissolved in deionized water (20 mL) containing 1-butyl-3-methylimidazolium hexafluorophosphate (0.1 g, $BmimPF_6$, Aldrich, 99%). The mixture was then heated to 120 °C for 18 h with stirring to evaporate water. The obtained white solid was ground using a mortar and pestle, and the white powder was dried under a vacuum for 12 h at room temperature (the obtained sample was denoted as MCP). The white powder was loaded into a quartz crucible and placed at the center of a tube furnace, and this was followed by several cycles of vacuum degassing and filling with N_2. The tube furnace was heated to 550 °C at a rate of 10 °C/min then held at this temperature for 4 h under an N_2 gas flow. After cooling to room temperature, the resultant product was obtained as a brownish-yellow powder. The powder (200 mg) was sonicated with an HCl solution (1 M, 150 mL) to remove the remaining impurities. The product was filtered using a membrane filter and washed several times with deionized water. Drying under vacuum for 12 h at room temperature afforded the final product, denoted as MCP-CN (1.6 g).

1.3. Measurement of the HER photocatalytic activity

The photocatalytic activity of the samples was measured in a top-irradiated vessel connected to a gas circulation system. The as-prepared powder sample (100 mg) with a Pt co-catalyst (3 mg) was dispersed in an aqueous solution of 10 vol% triethanolamine (100 mL,

TEOA) as a hole scavenger. The mixture was illuminated by visible-light irradiation from a Xe lamp (300 W, Newport Stratford Inc., USA) with an optical cutoff filter ($\lambda > 420$ nm). The amount of generated H_2 gas was quantified using gas chromatography (Shimadzu GC-2014, Japan).

1.4. Characterization

X-ray photoelectron spectroscopy (XPS) measurements were performed using a high-performance X-ray photoelectron spectrometer with a micro-focused monochromatic Al Kα X-ray source (1486.6 eV) operated at a spot size of 400 μm and 12 kV/72 W (K-Alpha+, Thermo Fisher Scientific, UK). X-ray diffraction (XRD) analysis was conducted using a multipurpose X-ray diffractometer (X'Pert powder diffractometer; Malvern Panalytical, UK). The Fourier transform infrared (FT-IR) spectrum of the sample in a KBr pellet was recorded using 64 scans on an FT-IR vacuum spectrometer (VERTEX 80 V, Bruker, Germany). The Brunauer−Emmett−Teller (BET) surface area and Barrett−Joyner−Halenda (BJH) pore size distribution of all samples were measured using an automatic physisorption analyzer (Micromeritics TriStar 3000, USA) via the N_2 adsorption-desorption at 77 K. Samples (0.2 g) were placed in a glass sample tube. To remove moisture and other adsorbed atmospheric gases from the surface, samples were heated at 250 °C and treated under vacuum for 6 h. Nitrogen isotherms were acquired from 2.0×10^{-5} to 0.99 (p/p°) relative pressure at −195.80 °C in liquid N_2. Transmission electron microscopy (TEM) images were obtained using a JEM-2100F instrument (JEOL, Japan) at 200 kV. The samples for TEM analysis were prepared by placing a droplet of the samples in a dimethylformamide suspension on a carbon-coated copper grid (LC300-Cu, Electron Microscopy Sciences) followed by drying. UV–Vis diffuse reflectance absorption spectra were obtained using a UV-2600 (Shimadzu, Japan) equipped with an ISR-2600 Plus integrating sphere attachment. TR-PL was measured with photoexcitation at 393 nm using a time-correlated single-photon counting (TCSPC) spectrometer (FluoTime 200, PicoQuant, Germany). Ultraviolet photoelectron spectroscopy (UPS) data were obtained using an AXIS Ultra DLD (Kratos, UK) under He I (21.2 eV) excitation sources, with Au foil as the reference. PL quantum efficiency (PLQE) was measured using a JASCO FP8500 spectrofluorometer with a 100-nm integrating sphere (ILF-835) and calculated in Jasco SpectraManager II Software.
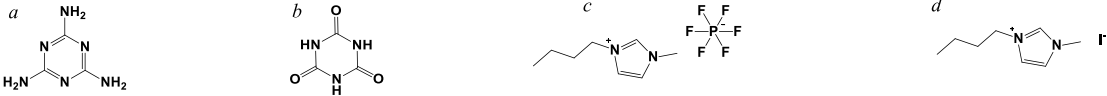
2. Results and discussion

2.1. Preparation of MCP-CN and morphological characterization

Melamine, which is one of the common precursors to produce 3D C_3N_4s, and cyanuric acid were reacted to form pre-organized intermediates in water. An ionic liquid ($BmimPF_6$) was mixed as a soft template and source of P dopant. The main product of this reaction is denoted as MCP-CN. Various combinations of the precursors were used to prepare control samples (M−CN, MC-CN, MP-CN, CP-CN, and MCI-CN, see Table 1).

Microscopic measurements revealed morphological variations depending on the combination of the precursors. As shown in the SEM and TEM images (Fig. 1 and Fig. S2), M−CN, which is a reference C_3N_4 material produced from melamine, possesses a flake-like morphology similar to that of typical bulk 3D C_3N_4 materials (Fig. 1b and c). In contrast, a tube-like morphology is observed in the images of MC-CN and MCP-CN (Fig. 1d–g, Fig. S2 and S3). The tubes have size distribution with an average length of 545 nm tubes are several mm (Fig. S2) in length and their outer diameter is approximately ~0.5 μm. The average wall thickness is ~22 nm, suggesting that the walls are composed of tens of layers (Fig. S3). In addition, porous morphology is observed at the tube walls of MCP-CN in the TEM images (Fig. 1d and e).

To understand the effect of precursor variations, three control samples (MC-CN, MP-CN, and CP-CN) were prepared by mixing two of the three precursor components (melamine, cyanuric acid, and $BmimPF_6$)

Table 1

The precursor compositions and their photocatalytic HER activity.

Samples		M-CN	MC-CN	MP-CN	CP-CN	MCP-CN	MCI-CN
Photocatalytic H_2 activity ($\mu mol \cdot h^{-1} \cdot g^{-1}$)		24.6	67.4	21.2	7.2	145.8	84.8
Precursors	Melamine [a] (M)	○	○	○	–	○	○
	Cyanuric acid [b] (C)	–	○	–	○	○	○
	Ionic liquid(P or I)	–	–	BmimPF$_6$ (P) [c]	BmimPF6 (P) c	BmimPF$_6$ (P) [c]	BmimI (I) [d]

a [structure: melamine with NH$_2$ groups on triazine ring]

b [structure: cyanuric acid]

c [structure: Bmim cation with PF$_6$ anion]

d [structure: Bmim cation with I anion]

(Table 1). As shown in Fig. 1, MC-CN is also a tube-type material; however, MCP-CN has better morphological uniformity than MC-CN. In contrast, the morphologies of MP-CN and CP-CN are similar to that of M−CN (Figs. S1a and d). These experiments suggest that tube morphology can be formed by polycondensation between melamine and cyanuric acid [24,25]. As another control for MCP-CN, the ionic liquid BmimPF$_6$ was replaced with BmimI, containing I$^-$ instead of PF$_6^-$. The resulting MCI-CN also exhibits a tube-like shape (Figs. S1e and f). Based on the TEM images of the MCP-CN and MCI-CN samples, the tube shape of MCP-CN is more uniform than that of MCI-CN, indicating that the type of ionic liquid is an important factor in controlling the morphology of the tubes.

The X-ray diffraction (XRD) pattern of MCP-CN shows fingerprint peaks at 12.8° and 27.7°, assignable to the distance between the intra-planar repeating tri-*s*-triazine building units and the interlayer distance of the C_3N_4 layers, respectively (Fig. 2a) [26,27]. This indicates the successful formation of the C_3N_4 structure in the MCP-CN nanotubes from a mixture of melamine, cyanuric acid, and BmimPF$_6$. While other control samples possess a similar pattern, CP-CN shows a shift of the peak at 27.7° and a decrease in intensity of the peak at 12.8°. This feature explains that the crystallinity of CP-CN is lower than other samples. The interlayer distance peak of MCP-CN possesses the lowest full width at half maximum (FWHM) value among the control samples, suggesting superior crystallinity of the MCP-CN (Table S1). The FT-IR spectrum of MCP-CN also shows features typical of common C_3N_4 materials (Fig. 2b). The peaks at 1641, 1573, 1462, and 1407 cm^{-1} correspond to heptazine-derived repeating structures [22]. The peaks at 1325 and 1239 cm^{-1} are assigned to completely condensed C–N and partially condensed C–NH moieties, respectively [17]. All the peaks at 1230–1650 cm^{-1} are sharper for MCP-CN than for the other samples. This supports a more homogeneous chemical environment in MCP-CN than in the others. Additional peaks for the breathing mode of the triazine rings and –NH$_x$ stretching modes are observed at 810 and 3000–3400 cm^{-1}, respectively [13,22].

BET measurements reveal that the samples (MC-CN, MCP-CN, and MCI-CN) generated from the co-use of melamine and cyanuric acid have a higher surface area than the others (Fig. 2c). The shape of N$_2$ adsorption and desorption isotherm curves of all samples is close to type II, suggesting the presence of macropores [28]. Additionally, the weak hysteresis in the curves indicates the formation of mesopores in some degree. MCP-CN has the highest surface area of 66 m^2 g^{-1} and the largest average pore volume of 0.4 m^2 g^{-1}. The N$_2$ desorption curves of the MCP-CN, MC-CN, and MCI-CN samples show the presence of mesopores with diameters of 20–40 Å, while the other samples contain pores with a broader range of diameters (Fig. 2d). Based on microscopic characterization, it can be deduced that the co-use of melamine and cyanuric acid causes the formation of tubular C_3N_4 materials containing porous structures.

2.2. Chemical characterizations of MCP-CN

Various analyses were carried out to understand the chemical structure of the MCP-CN nanotubes based on a comparison with common C_3N_4 (M−CN). ^{1}H, ^{13}C, and ^{15}N cross-polarization magic-angle spinning (CP-MAS) SSNMR measurements with MCP-CN and M−CN elucidated their detailed chemical structure (Fig. 3). The deconvoluted ^{13}C SSNMR spectra show three major peaks at 156.9, 162.9, and 165.3 ppm, corresponding to internal C atoms in tri-*s*-triazine rings (C$_i$), C atoms next to bridging –NH– (C$_b$), and a combination of C atoms (C$_t$) bonded to terminal NH$_2$ and internal C atoms (C$_h$) adjacent to N atoms with H bonds, respectively (Fig. 3a) [29–31]. Five N-associated species, namely, C=N–C (N$_c$), N–C$_3$ (N$_i$), C(NH)C (N$_b$), –NH$_2$ with H bonds (N$_{h-t}$), and –NH$_2$ (N$_t$) groups without H bonds, are observed at 192.2, 155.8, 135.3, 116.8, and 106.9 ppm, respectively, in the ^{15}N SSNMR spectra (Fig. S4) [30]. The deconvoluted ^{1}H SSNMR spectra show four peaks at 11.7, 8.9, 6.2, and 4.1 ppm of bridging -NH- groups with (H$_{h-b}$) and without (H$_b$) H bonds and terminal –NH$_2$ groups with (H$_{h-t}$) and without (H$_t$) H bonds (Fig. 3b) [13,29]. These measurements reveal that the MCP-CN nanotubes are composed of tri-*s*-triazine structures.

The SSNMR spectra of MCP-CN were compared with those of M−CN to examine changes in the chemical structure during the formation of the tubes. Although the ^{1}H, ^{13}C, and ^{15}N SSNMR spectra of MCP-CN are similar to those of M−CN, there are distinct features indicating structural differences. In the deconvoluted ^{13}C SSNMR spectra, the C$_b$ peak of MCP-CN increases significantly in intensity compared to that of M−CN (Fig. 3a and Table S2). This suggests that MCP-CN contains more bridging –NH groups linking the tri-*s*-triazine rings than M−CN does. The deconvoluted ^{15}N and ^{1}H SSNMR spectra of MCP-CN show an obvious decrease in the intensity of the N$_t$ and H$_t$ peaks, respectively, relative to those of M-CN. (Table S3). All these features reveal that a significant portion of the edge –NH$_2$ groups are removed during the formation of MCP-CN nanotubes. Combined with the ^{13}C SSNMR measurements, the evidence suggests that –NH– bridging groups are formed from the condensation reactions between –NH$_2$ groups at the edges of C_3N_4 domains, resulting in the formation of C_3N_4 nanotubes containing more –NH– linkages between the edge sites of the C_3N_4 layers.

The XPS data further support the SSNMR characterization. The deconvoluted XPS C 1*s* spectra of MCP-CN and M−CN show the main peak at 288.0 eV, corresponding to N–C=N moieties in tri-*s*-triazine rings, and minor peaks at 288.4, 286.3, and 284.6 eV, corresponding to C–NH$_2$, C–O, and C=C/C–C groups, respectively (Fig. 3c) [32]. The C=C/C–C peak originates from C-containing impurities, which can be produced during high-temperature processes [26]. It leads the higher C/N values of materials than the theoretical value (0.75) of C_3N_4 structure (Table S4). The XPS peak intensity and a C/N value are smaller for MCP-CN than for M−CN, suggesting that MCP-CN contains fewer C impurities. This is supported by the XRD data showing better crystallinity of MCP-CN.

The deconvoluted N 1*s* spectra of both samples exhibit typical features of C_3N_4 materials with peaks at 398.4, 399.9, and 401.0 eV, which can be assigned to C=N=C, N–(C)$_3$, and –NH$_x$ groups, respectively (Fig. 3d) [22]. The N–(C)$_3$ and –NH$_x$ groups are located inside and at the edges of the tri-*s*-triazine rings, respectively. Consequently, a larger N–(C)$_3$/–NH$_x$ ratio indicates the presence of fewer edge sites. As shown in Table S5, this ratio for MCP-CN, calculated from the deconvoluted XPS N 1*s* spectrum, is larger than that for M-CN. These data support the
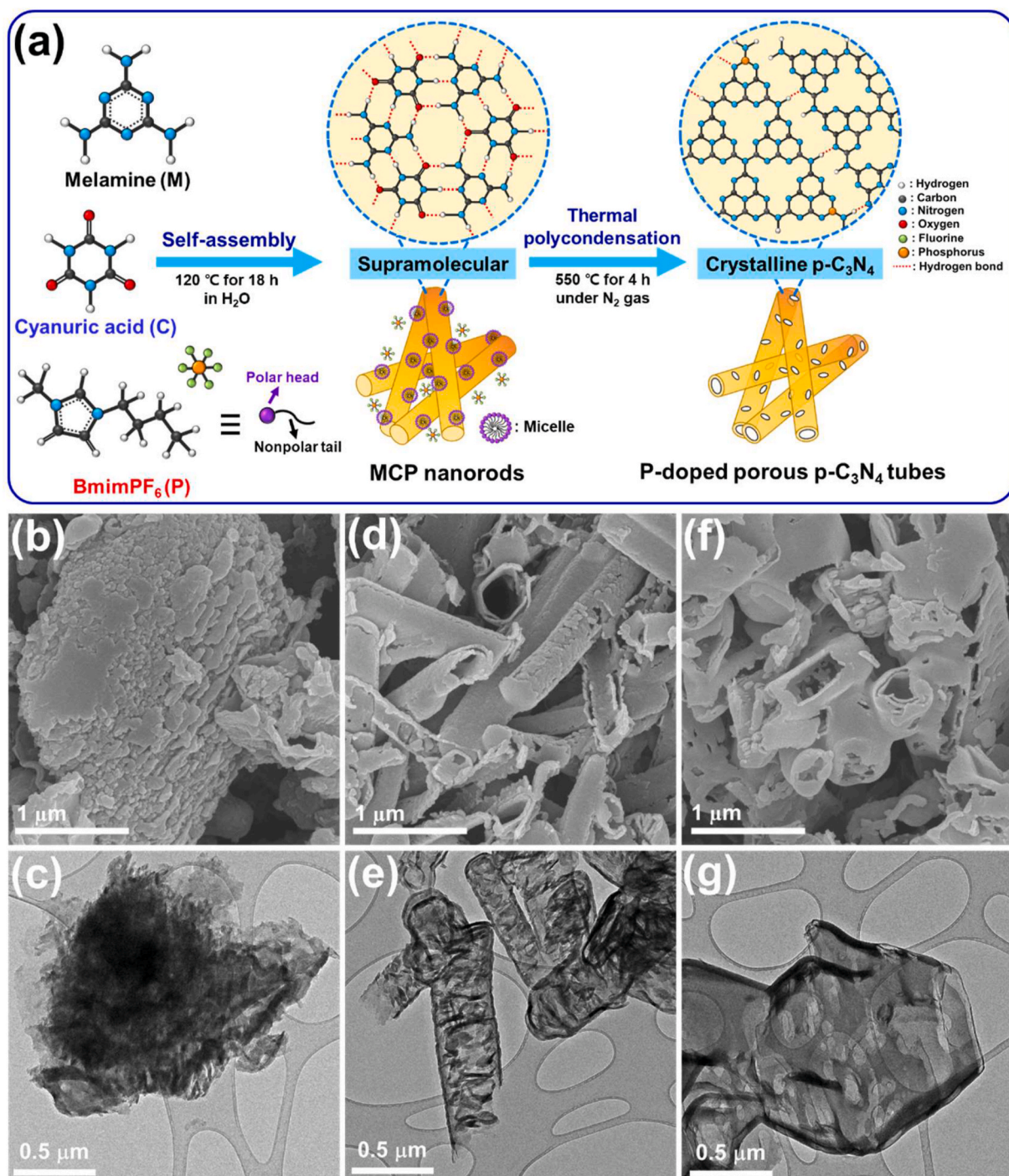
Fig. 1. (a) Scheme for MCP-CN preparation SEM images of (b) M−CN, (d) MCP-CN, and (f) MC-CN. TEM images of (c) M−CN, (e) MCP-CN, and (g) MC-CN. (A colour version of this figure can be viewed online.)

presence of fewer edges in the MCP-CN than in the M-CN. As explained above, the SSNMR characterizations suggest a similar feature, which is the presence of more –NH– linkages between edge sites of C_3N_4 layers in the MCP-CN tube than in M-CN.

The P-associated chemical structure was investigated by ^{31}P SSNMR and P 2*p* XPS analyses. The elemental amount of P in MCP-CN is 0.7 at%, as determined by XPS measurements (Table S4). The ^{31}P SSNMR spectrum of MCP-CN shows a broad peak pattern because of the small number of P atoms and the presence of multiple P-containing species (Fig. 3e). The region between 0 and −40 ppm can be assigned to P atoms replacing corner C atoms at terminal sites of the tri-*s*-triazine network

[33,34]. Although there are two replaceable C sites (Corner-C and Bay-C), P atoms would replace Corner-C atoms rather than Bay-C atoms. Previous theoretical calculations have suggested that the replacement of Corner-C sites with P atoms is energetically favorable relative to that of Bay-C sites [35]. The deconvoluted P 2*p* XPS spectrum of MCP-CN also supports the presence of P–N bonds, with a major peak at 133.4 eV (Fig. 3f) [36,37].

2.3. Mechanistic study of tube structure formation

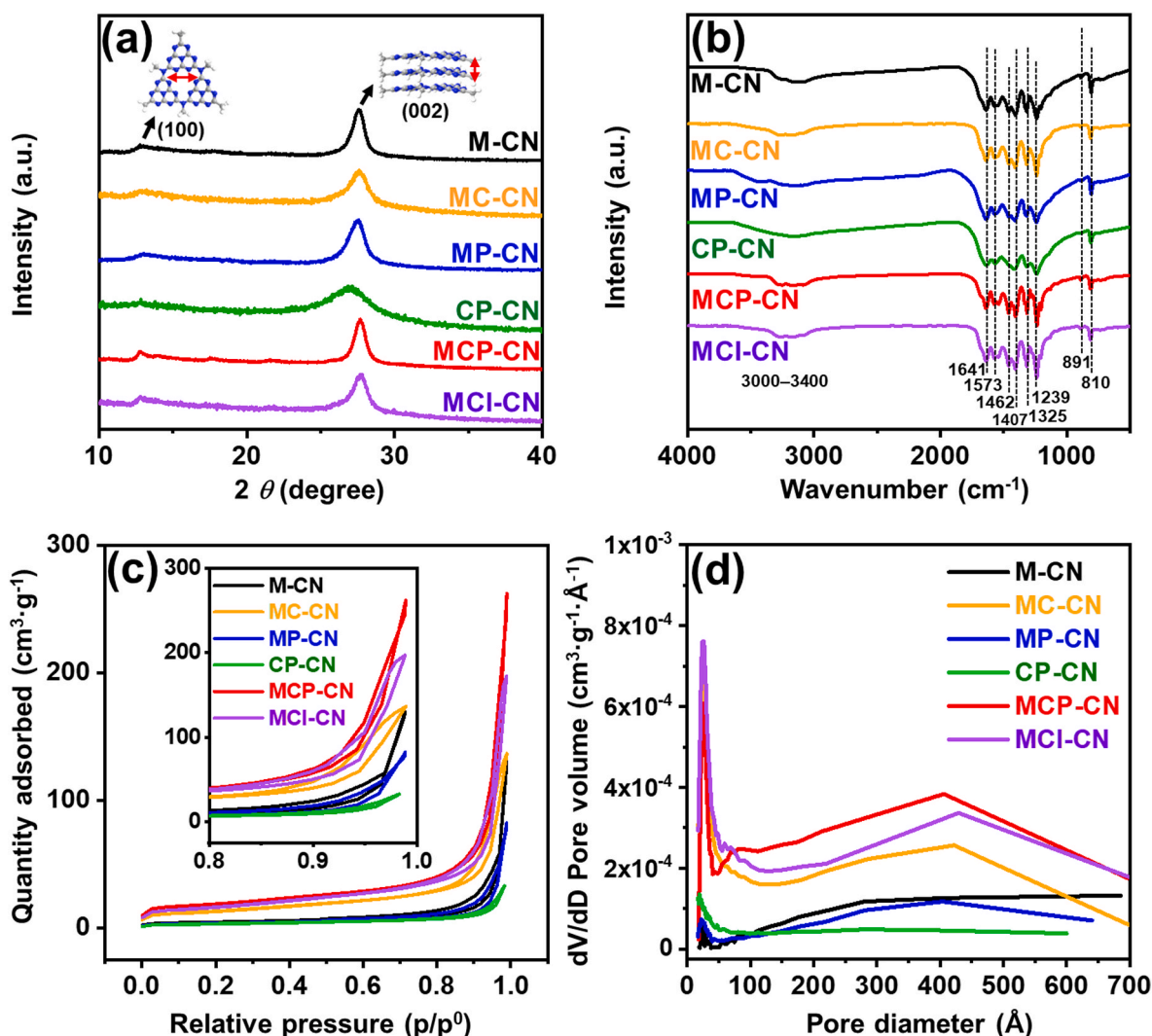As mentioned above, the tube materials (MC-CN and MCP-CN) were

Fig. 2. (a) XRD patterns, (b) FT-IR spectra, (c) N_2 absorption/desorption isotherms (inset: a magnified image), and (d) BJH pore size distribution of M−CN, MC-CN, MP-CN, CP-CN, MCP-CN, and MCI-CN. (A colour version of this figure can be viewed online.)

produced from melamine and cyanuric acid. Control experiments were performed to elucidate the formation mechanism. A mixture of melamine, cyanuric acid, and $BmimPF_6$ was dissolved in water and treated at 120 °C. During this process, water was evaporated, yielding the MCP intermediate as a powder (Fig. 1a; see the experimental section for the preparation of other intermediates (M, C, MC, and CP) in SI). The isolated MCP intermediate was then analyzed.

Interestingly, TEM images of MCP intermediates reveal the presence of a rod-shaped material 1–2 μm in length and 0.4–0.5 μm in diameter (Fig. 4a and b). The XRD pattern of the MCP intermediates is significantly different from that of MCP-CN and similar to that of melamine cyanurate (Fig. 4c) [38,39]. This indicates the formation of melamine cyanurate rather than C_3N_4 structure at the MCP intermediate stage.

The XRD pattern of the MCP intermediate is highly similar to that of the MC intermediate (Fig. S5), suggesting the formation of a self-assembled structure, such as melamine cyanurate, between melamine and cyanuric acid. The peak at ~27° in the pattern of MCP-CN is shifted to a slightly lower angle relative to that of the MCP intermediate, indicating that the interlayer distance between the C_3N_4 layers in MCP-CN is slightly larger than the distance between the π-conjugated rings in the MCP intermediate. While the intraplanar distance between the tri-*s*-triazine rings is observed at 13° for MCP-CN, the MCP intermediate shows a peak at a lower angle. This could be explained by the longer distance between interplanar rings in the self-assembled intermediate,

which is formed by the hydrogen bonding of melamine and cyanuric acid.

The FT-IR spectrum of the MCP intermediate shows characteristic peaks for melamine cyanurate at 3396 and 3234 cm^{-1}, corresponding to the symmetric and asymmetric stretching of amine groups with H-bonds, respectively [40]. This feature suggests the formation of H-bonds between the amine groups of the melamine and the O atoms of cyanuric acid. The other peaks at 1782, 1743, 1528, and 1449 cm^{-1} correspond to C═O, –NH$_2$, C═N, and C–N stretching, respectively. The peak at 1667 cm^{-1} is assignable to the NH$_2$ bending mode [41–43]. After heat treatment, MCP-CN exhibits different spectral characteristics from those of the MCP intermediate. The H-bonding peaks are still present but are weaker in intensity, and the typical peak pattern of the C_3N_4 network is observed. From these observations, it can be deduced that the rod materials (MCP intermediates) are formed through the self-assembly of melamine and cyanuric acid during the treatment at 120 °C in water. Previous literatures suggest that H bonding is a critical driving force to form self-assembled frameworks between building units [44–48]. Then, during the 550 °C treatment, porous C_3N_4 tubes (MCP-CN) are generated by polycondensation of the intermediates.

The XRD patterns of the MC and MCP intermediates are almost identical (Fig. S5), indicating that the addition of $BmimPF_6$ does not significantly affect the self-assembled structure of the intermediates. However, as discussed above, the porosity and surface area of the C_3N_4
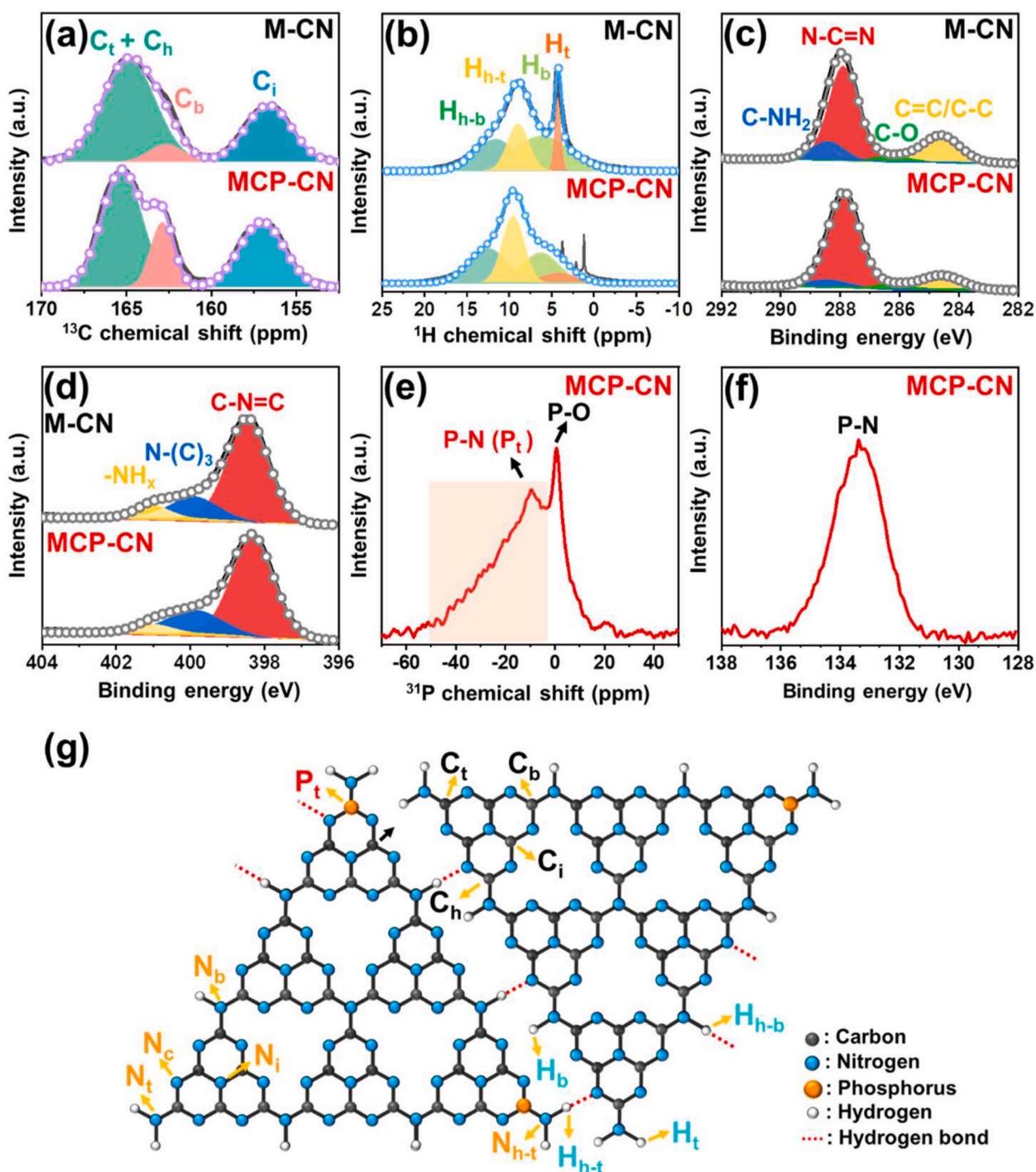
Fig. 3. CP-MAS SSNMR spectra of M−CN and MCP-CN (a) ^{13}C and (b) ^{1}H. Deconvoluted XPS spectra of M−CN and MCP-CN: (c) C 1s and (d) N 1s. (e) ^{31}P SSNMR spectrum and (f) XPS P 2p spectrum of MCP-CN. (g) A proposed chemical structure of MCP-CN. (A colour version of this figure can be viewed online.)

samples varied with the addition of ionic liquids, which is similar to previous literatures [35,49–51]. Since BmimPF$_6$ is amphiphilic, micelles would be formed in the aqueous medium. When nanorods are generated from a mixture consisting of melamine and cyanuric acid, the BmimPF$_6$ micelles can be dispersed on the surface of the nanorods through H bonding between the ionic liquid and terminal H atoms of the MCP intermediates [52–54]. During the 550 °C treatment, some bubbles are generated by the thermal decomposition of BmimPF$_6$, resulting in the formation of a porous structure. Simultaneously, phosphorus atoms can be incorporated into the C$_3$N$_4$ network by replacing corner C atoms to produce P-doped C$_3$N$_4$ nanotube materials (MCP-CN).

2.4. Photocatalytic HER performance and photophysical characterization of MCP-CN

To utilize the MCP-CN nanotubes, their photocatalytic properties for H$_2$ evolution were investigated under visible-light irradiation. The HER is a necessary step in the water-splitting process, which is required for eco-friendly H$_2$ production. The development of efficient photocatalysts that can utilize sustainable solar energy to induce the HER is one of the key challenges in producing H$_2$ without the use of fossil fuels. Because sunlight at Earth's surface contains ~43% visible light, it is essential to develop visible-light-active photocatalysts to achieve high catalytic
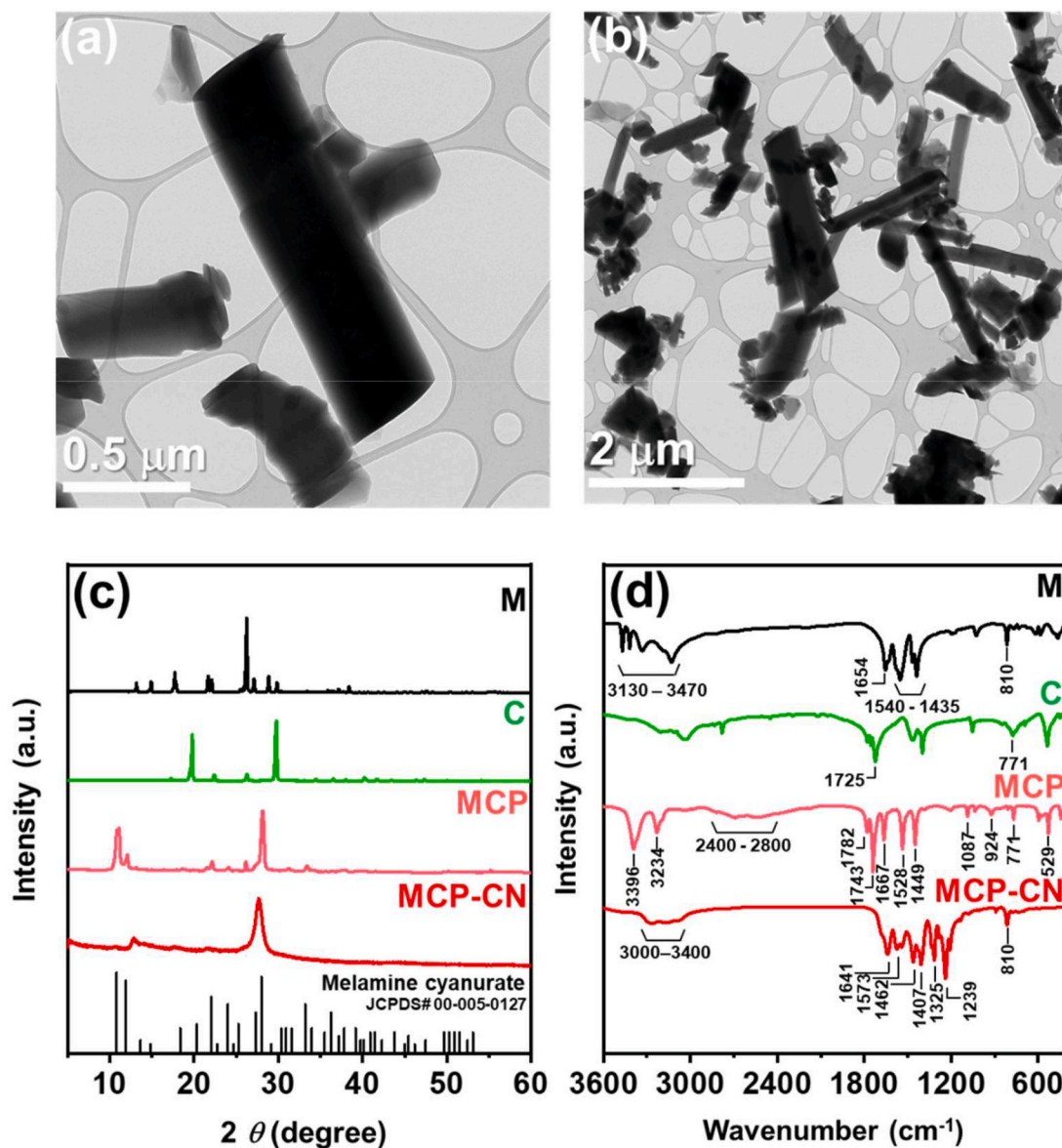
Fig. 4. (a) and (b) TEM images of the MCP intermediates at different magnifications. (c) XRD pattern and (d) FT-IR spectra of M, C, MCP, and MCP-CN samples. (A colour version of this figure can be viewed online.)

efficiency [55].

Pt and TEOA (10 vol%) were used as the co-catalyst and hole scavenger, respectively. Fig. 5a and Table 1 show the photocatalytic activities, which are defined as the amount of H_2 molecules normalized by the reaction time and mass of the used catalysts. As shown in Fig. 5, the MCP-CN exhibits excellent photocatalytic HER activity of 145.8 μmol $h^{-1}g^{-1}$, which is approximately 6 times higher than that (24.6 μmol $h^{-1}g^{-1}$) of the common C_3N_4 material, M-CN. As shown in Fig. 5b, MCP-CN exhibited superior photocatalytic activity compared to the other control samples. Furthermore, it indicates that MCP-CN is a more efficient photocatalyst than bulk C_3N_4 photocatalysts reported previously (Table S6). To confirm the stability of MCP-CN during the photocatalytic HER reactions, cyclic tests with MCP-CN and TEM measurements with MCP–CN–after-test were done. Fig. 5c shows that photocatalytic HER activity of MCP-CN maintains during consecutive four cycles. TEM images of MCP–CN–after-test sample exhibit the preservation of tubular morphology after photocatalytic reactions (Fig. 5d). These data indicate that MCP-CN is stable in the photocatalytic reaction conditions.

Interestingly, the tube-like materials (MCP-CN, MC-CN, and MCI-CN) show higher activities than other materials (M−CN, MP-CN, and

CP-CN). As mentioned above, the former has a higher surface area and more porous structure than the latter. Consequently, these morphological features are important for enhanced photocatalytic HER activity. Among the tube-like materials, MCP-CN is the most efficient catalyst, with significantly superior activity. Compared with the tube-like materials, the surface area of MCP-CN is 43 and 15% higher than those of MC-CN and MCI-CN, respectively. However, the photocatalytic activity of MCP-CN is 116 and 72% higher than those of MC-CN and MCI-CN, respectively. In other words, the enhancement of the photocatalytic activity is much larger than that of the surface area. Consequently, there are additional reasons for the superior photocatalytic performance of the MCP-CN.

To understand the superior activity of MCP-CN, the photophysical properties of M−CN, MC-CN, and MCP-CN were characterized by absorption, PL, time-resolved PL, and 2D EEM, providing both static PL and PL excitation (PLE) spectra. Fig. 6a and Fig. S6a show the absorption spectra, and their bandgaps were calculated using the Kubelka-Munk function from the diffuse reflectance spectra (DRS), as shown in Fig. 6b and S6c-h. The conduction band (CB) positions of M−CN, MC-CN, MP-CN, CP-CN, MCP-CN, and MCI-CN were determined to be
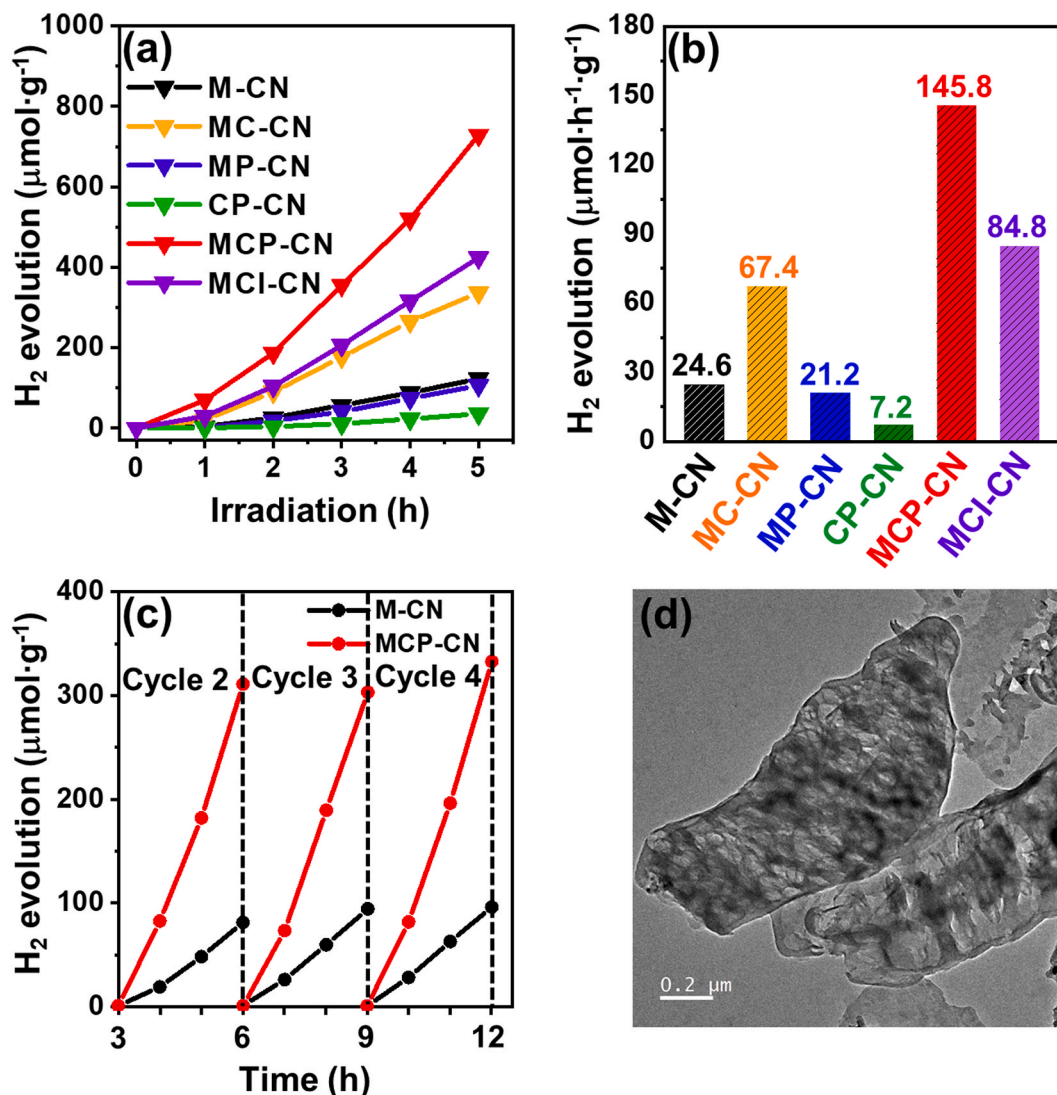
Fig. 5. (a) Photocatalytic activities for H_2 evolution and (b) time-normalized photocatalytic H_2 production rates of all samples under visible-light irradiation ($\lambda >$ 420 nm) for 5 h, (c) cycle tests for photocatalytic H_2 evolution of M−CN and MCP-CN, and (d) TEM image MCP–CN–after-test sample. (A colour version of this figure can be viewed online.)

−0.65, −0.53, −0.70, −0.56, −0.59, and −0.55 V vs. the normal hydrogen electrode (NHE), respectively, from Mott-Schottky plots and the derived flat-band potentials (E_{fb}) in Fig. S6b. All samples have conduction band edges located at suitable energies to reduce H^+ to H_2 (Fig. 6c and Fig. S6i).

As shown in the absorption spectra (Fig. 6a), it is revealed that P-doping affects the light absorption features of C_3N_4 materials. Specifically, M−CN, MC-CN, and MCP-CN commonly exhibit strong absorption at <400 nm, corresponding to the $\pi \rightarrow \pi^*$ transition [17]. In addition to the transition, MCP-CN shows an extra absorption peak at ~500 nm, which can be assigned to the n $\rightarrow \pi^*$ transition [56,57]. The presence of this transition suggests that MCP-CN has mid-gap states, in contrast to those of M−CN and MC-CN. In the inset of Fig. 6b, the transition energy from the valence band (VB) to the mid-gap states for MCP-CN was calculated to be 1.97 eV by the Kubelka-Munk function from the DRS. The mid-gap states are also observed in previous literatures reporting P-doped C_3N_4 materials [35,50,51]. Theoretical calculation suggests that empty mid-gap states can be formed by the hybridization of C $2s2p$, N $2s2p$ and P $3s3p$ [49]. Also, possible defects and the breakage of centrosymmetric structures associated with P-doping would be additional reasons for the mid-states. Therefore, it can be implied that P-doping into the C_3N_4 network modifies the electronic structure of the

photocatalyst and leads to an increase in the visible-light absorption ability. Such a modification should be beneficial for improving the photocatalytic activities because the HER activity is measured under visible-light irradiation.

To study the dynamics of the photo-excited charge carriers, TR-PL spectroscopy was performed for M−CN, MC-CN, and MCP-CN. Each TR-PL decay was fitted with three exponential functions (Fig. 6d and Fig. S7). The individual time constants τ_1, τ_2, and τ_3 correspond to the recombination, intralayer migration, and interlayer migration of the charge carriers, respectively (Table S7) [58]. The average PL lifetimes were calculated from the time constants and amplitudes of the three exponential components. The PL lifetimes of the tube-like materials (MC-CN and MCP-CN) are similar. Interestingly, they show much slower PL decay than M−CN, especially for the τ_3. A PLQE of MCP-CN powder, which was measured with 280 nm excitation, was determined to be 5.4%. This value is somewhat smaller than other C_3N_4-based materials previously reported [59]. The longer lifetime of the charge carriers and low PLQE in MCP-CN sample enhances their usefulness for the photocatalytic HER. The results of the TR-PL measurements are further supported by the photocurrent responses of M−CN and MCP-CN using sequential on-off visible-light irradiation. MCP-CN generated a much higher current density than M−CN, indicating facile separation of the
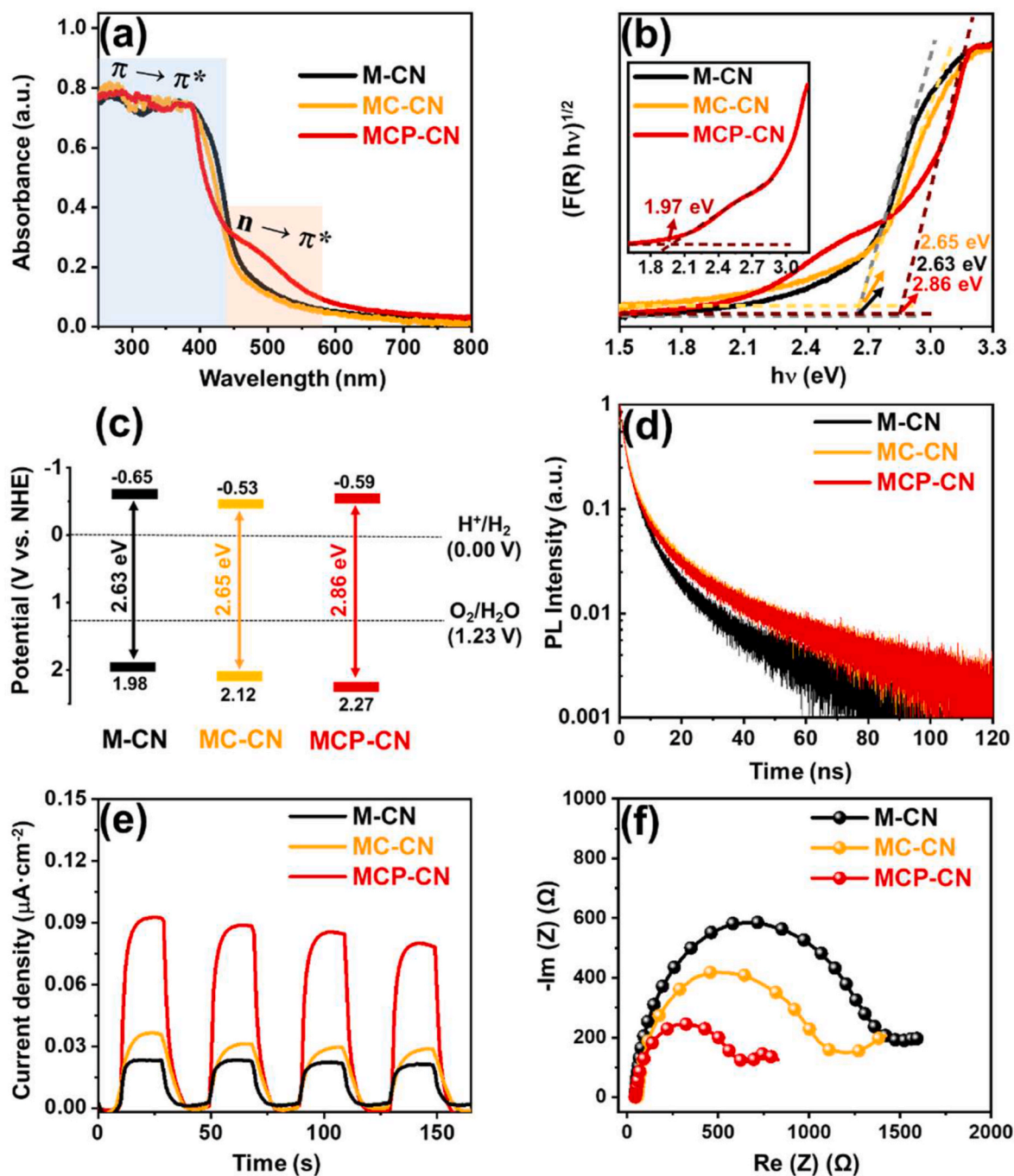
Fig. 6. (a) Absorption spectra, (b) Kubelka-Munk plots of diffuse reflectance spectra for band gaps, (c) band structure diagrams of M−CN, MC-CN, and MCP-CN. (d) Time-resolved PL decays of M−CN, MC-CN, and MCP-CN measured at the major peak of each PL spectrum under 393 nm excitation. (e) Photocurrent response of M−CN, MC-CN, and MCP-CN measured under on/off visible-light irradiation. (f) Nyquist plots obtained from EIS measurements for M−CN, MC-CN, and MCP-CN. (A colour version of this figure can be viewed online.)

photogenerated charge carriers (Fig. 6e and Fig. S7b). From the Nyquist plots obtained using electrochemical impedance spectroscopy (EIS) data (Fig. 6f and Fig. S7c), it is revealed that MCP-CN has the lowest charge transfer resistance (R_{ct}), implying the fastest charge transfer at the interfaces in MCP-CN.

The 2D EEM spectra, which display the correlation between the excitation and emission characteristics, were measured for all the powder samples (Fig. 7a–c and S8a–c). The PLE spectra were extracted from the 2D EEM spectra to understand the absorption features related to the emission properties at a specific wavelength. Fig. 7d and Fig. S8d shows the PLE spectra extracted by integrating the 2D EEM spectrum

along the emission-wavelength axis. All spectra show absorption peaks at 275 and 370 nm, corresponding to the $\pi \to \pi*$ transition [60]. The spectrum of M−CN shows a broad spectral feature at 400–450 nm, which suggests the presence of other $\pi \to \pi*$ transition C_3N_4 domains [13]. This absorption feature significantly decreases in MC-CN and MCP-CN, suggesting the more homogenous $\pi \to \pi*$ transition C_3N_4 domains in MC-CN and MCP-CN. This feature can be explained with chemical structures mentioned above. MCP-CN has more bridging –NH groups linking the tri-s-triazine rings than M-CN. The bridging groups are formed from the condensation reactions between –NH$_2$ groups at the edges of C_3N_4 domains. This could lead the formation of C_3N_4 domains
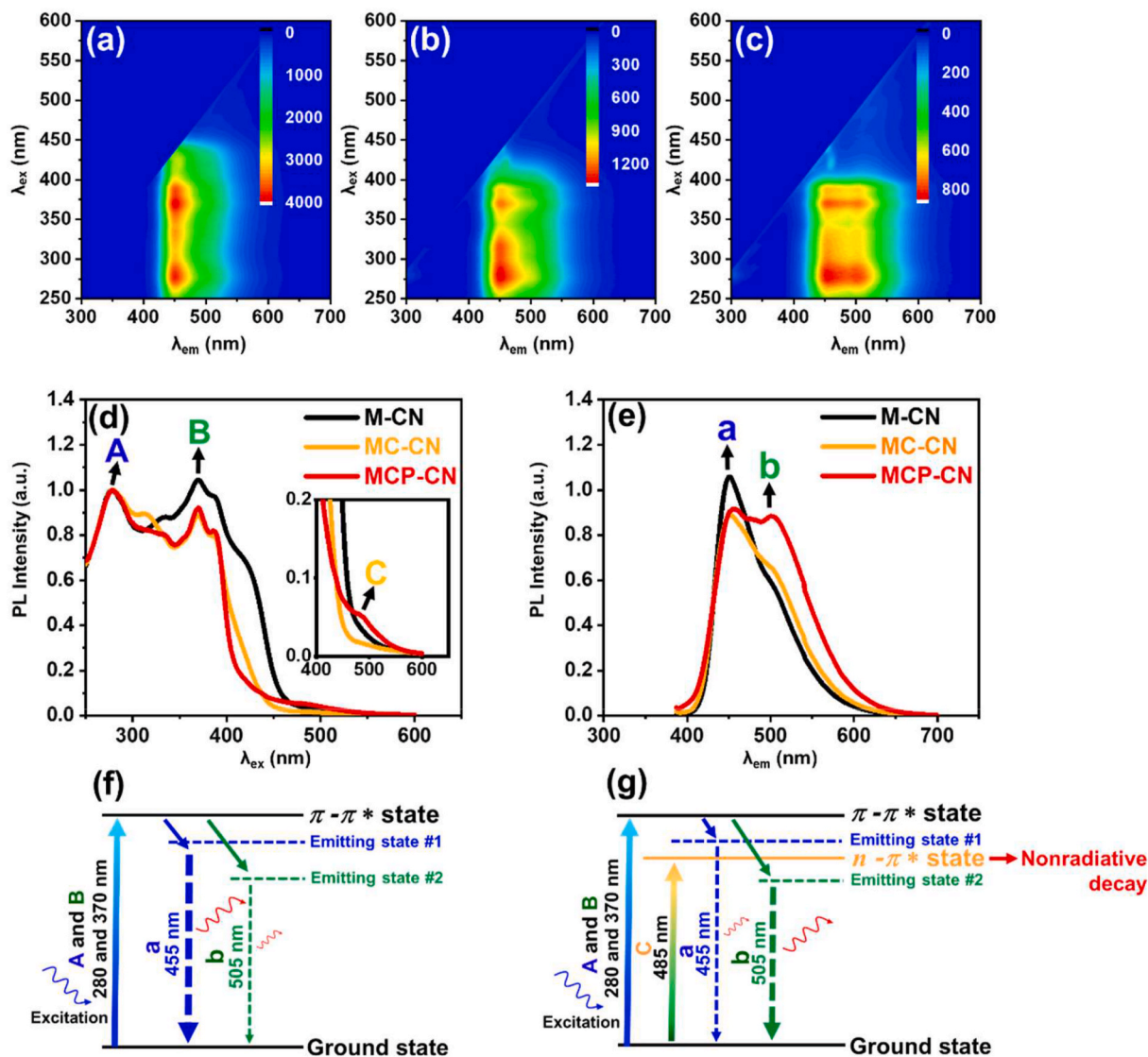
Fig. 7. 2D EEM spectra of (a) M−CN, (b) MC-CN, and (c) MCP-CN. (d) Integrated PLE spectra of M−CN, MC-CN, and MCP-CN extracted from the 2D EEM spectra. (e) Normalized PL spectra of M−CN, MC-CN, and MCP-CN with 370 nm excitation extracted from the 2D EEM spectra. Proposed energy level diagram of (f) M−CN and (g) MCP-CN. (A colour version of this figure can be viewed online.)

with narrower size distribution and better crystallinity, resulting in the narrow light absorption feature for $\pi \rightarrow \pi^*$ transition.

While the PLE spectra of M−CN and MC-CN show almost identical spectral features to those observed in the absorption spectra (Fig. 6a), MCP-CN exhibits a unique feature at ~500 nm, as shown in the inset of Fig. 7d. As mentioned above, the UV–Vis absorption spectrum of MCP-CN shows the same absorption feature corresponding to the $n \rightarrow \pi^*$ transition. However, this absorption feature is much less distinct in the PLE spectrum of MCP-CN. This contrast in the intensity of the ~500 nm absorption feature in the absorption and PLE spectra implies that the charge carriers generated by this transition might relax through non-radiative decay pathways, as shown in Fig. 7g. In other words, the charge carriers generated by the $n \rightarrow \pi^*$ transition do not contribute to the emission and are transferred to participate in the photocatalytic HER.

Fig. 7e and Fig. S8e show the PL spectra of all the samples extracted from the 2D EEM spectra at an excitation wavelength of 370 nm. Two emission peaks are observed at 455 and 505 nm (a and b), which could be related to the $\pi \rightarrow \pi^*$ transition [13]. Based on comparing the spectra of M−CN, MC-CN, and MCP-CN, MCP-CN shows a decrease in the 455-nm peak and an increase in the 505-nm peak relative to the other

samples. This feature is likely to reflect structural changes, such as the higher crystallinity and larger domain size of MCP-CN. Based on the photophysical characterization, proposed energy-level diagrams for M−CN and MCP-CN are displayed in Fig. 7f and g.

2.5. Further insight into the photocatalytic properties of MCP-CN nanotubes

As discussed above, the chemical and morphological structure of MCP-CN can be characterized by comparison with that of the other control samples. The MCP-CN nanotubes showed the highest photo-catalytic activity for the HER among all the samples (Table 1). In this section, further insight into the photocatalytic behavior of MCP-CN is discussed based on its relationship with the structural features.

The band gaps and CB edge energies of the materials are suitable for absorbing visible light and for the HER, respectively. BET measurements revealed that the MCP-CN nanotubes possessed macropores and the highest surface area and pore volumes among the samples. Previous study suggested that the microporous structure in C_3N_4 materials can improve photocatalytic properties due to enhanced light harvesting by multiple scattering effect and the facile transfer of reactants through the

porous network [49]. the Consequently, the high surface area of the catalysts is one of the major reasons for their superior photocatalytic activity. Possible access to both the interior and exterior surfaces of the nanotubes would lead to a higher surface area.

However, as mentioned above, the photocatalytic activity of MCP-CN was much higher than that of the other tube-type samples despite their relatively similar degrees of surface area. Consequently, additional factors must be attributable to the chemical structure. Various spectroscopic analyses revealed that –NH– bridging groups are formed between the –NH_2 groups at the edges of the C_3N_4 domains in MCP-CN. This leads to the formation of MCP-CN nanotubes containing larger domains with more –NH– linkages between the edge sites of the C_3N_4 layers. Previous studies have suggested that a larger domain size with amine bridges is beneficial for facile intralayer transfer of photoexcited charge carriers [13]. This is also supported by our experiments, such as the longer PL lifetimes, higher photocurrents, and lower resistance at the interfaces of the MCP-CN nanotubes. Additionally, the improved crystallinity of the C_3N_4 structure and the low amounts of C impurities in MCP-CN could be other reasons for the facile intralayer transfer. Additionally, the improved electric properties could be attributed to P-doping into C_3N_4 network as suggested by previous study [33,50,61].

XPS and SSNMR studies indicated the incorporation of P atoms into the C_3N_4 networks. MCP-CN showed a distinct enhancement of the n → π* transition relative to the other tube (MC-CN) and flake (M−CN) materials, as discussed above. Our study suggests that this feature is induced by the presence of mid-gap states. Previous reports also suggest that P-doping into C_3N_4 network generates the mid-gap states and decrease energy level gaps [35,49,50,56]. It leads that MCP-CN has a higher visible-light absorption ability than the other samples. This is another reason for the superior visible-light-active photocatalytic behavior of MCP-CN.

3. Conclusions

In this study, one-dimensional (1D) P-doped carbon nitride nanotubes (MCP-CN) were designed via supramolecular self-assembly between melamine and cyanuric acid. The use of an ionic liquid (1-butyl-3-methylimidazolium hexafluorophosphate) produced nanotubes with uniform morphology. The control experiments suggest that rod-shaped intermediates are formed by self-assembly of melamine and cyanuric acid then porous MCP-CN are generated by polycondensation of the intermediates.

MCP-CN showed an excellent photocatalytic HER activity of 145.8 μmol $h^{-1}g^{-1}$ under visible-light irradiation. From comprehensive experimental studies with various control samples, we can understand the relationship between the photocatalytic activity, 1D nanotube morphology, chemical and P-doping structures, and photophysical properties of the MCP-CN nanotubes. This study provides a new route for producing 1D C_3N_4 nanotubes with P doping. Furthermore, our new structural and photocatalytic insights are useful for rational control of the photocatalytic properties of C_3N_4 materials.

CRediT authorship contribution statement

Dawoon Jang: Conceptualization, Investigation, Validation, Formal analysis, Writing – original draft. **Suyeon Lee:** Conceptualization, Investigation, Formal analysis, Writing – review & editing. **Nam Hee Kwon:** Investigation, Validation, Writing – review & editing. **Taehoon Kim:** Investigation, Validation, Formal analysis. **Sangjoon Park:** Investigation, Validation, Formal analysis. **Kyung Yeon Jang:** Validation, Formal analysis. **Eojin Yoon:** Formal analysis. **Seungjoo Choi:** Formal analysis. **Juheon Han:** Formal analysis. **Tae-Woo Lee:** Writing – review & editing. **Jeongho Kim:** Writing – review & editing. **Seong-Ju Hwang:** Conceptualization, Validation, Writing – review & editing, Funding acquisition, Supervision, Project administration. **Sungjin Park:** Conceptualization, Validation, Writing – review & editing, Funding acquisition, Supervision, Project administration.

Declaration of competing interest

The authors declare the following financial interests/personal relationships which may be considered as potential competing interests: Seong-Ju Hwang reports financial support was provided by National Research Foundation of Korea. Sungjin Park reports financial support was provided by National Research Foundation of Korea. Sungjin Park reports a relationship with Inha University that includes: employment.

Acknowledgements

Appendix A. Supplementary data

Supplementary data to this article can be found online at https://doi.org/10.1016/j.carbon.2023.03.038.

References

[1] P. Audebert, E. Kroke, C. Posern, S.-H. Lee, State of the art in the preparation and properties of molecular monomeric s-heptazines: syntheses, characteristics, and functional applications, Chem. Rev. 121 (2021) 2515–2544, https://doi.org/10.1021/acs.chemrev.0c00955.

[2] I.F. Teixeira, E.C. Barbosa, S.C.E. Tsang, P.H. Camargo, Carbon nitrides and metal nanoparticles: from controlled synthesis to design principles for improved photocatalysis, Chem. Soc. Rev. 47 (2018) 7783–7817, https://doi.org/10.1039/c8cs00479j.

[3] Z. Teng, Q. Zhang, H. Yang, K. Kato, W. Yang, Y.-R. Lu, S. Liu, C. Wang, A. Yamakata, C. Su, Atomically dispersed antimony on carbon nitride for the artificial photosynthesis of hydrogen peroxide, Nat. Catal. 4 (2021) 374–384, https://doi.org/10.1038/s41929-021-00644-8.

[4] C. Hu, F. Chen, Y. Wang, N. Tian, T. Ma, Y. Zhang, H. Huang, Exceptional cocatalyst-free photo-enhanced piezocatalytic hydrogen evolution of carbon nitride nanosheets from strong in-plane polarization, Adv. Mater. 33 (2021), 2101751, https://doi.org/10.1002/adma.202101751.

[5] J. Zhang, Y. Li, X. Zhao, L. Wang, H. Chen, S. Wang, X. Xu, L. Shi, L.-C. Zhang, Y. Zhu, Aligning potential differences within carbon nitride based photocatalysis for efficient solar energy harvesting, Nano Energy 89 (2021), 106357, https://doi.org/10.1016/j.nanoen.2021.106357.

[6] J. Barrio, M. Volokh, M. Shalom, Polymeric carbon nitrides and related metal-free materials for energy and environmental applications, J. Mater. Chem. 8 (2020) 11075–11116, https://doi.org/10.1039/D0TA01973A.

[7] V.W.h. Lau, B.V. Lotsch, A tour-guide through carbon nitride-land: structure-and dimensionality-dependent properties for photo (electro) chemical energy conversion and storage, Adv. Energy Mater. 12 (2022), 2101078, https://doi.org/10.1002/aenm.202101078.

[8] S. Seok, D. Jang, H. Kim, S. Park, Production of NiO/N-doped carbon hybrid and its electrocatalytic performance for oxygen evolution reactions, Carbon Lett. 30 (2020) 485–491, https://doi.org/10.1007/s42823-019-00118-9.

[9] X. Wang, K. Maeda, A. Thomas, K. Takanabe, G. Xin, J.M. Carlsson, K. Domen, M. Antonietti, A metal-free polymeric photocatalyst for hydrogen production from water under visible light, Nat. Mater. 8 (2009) 76–80, https://doi.org/10.1038/nmat2317.

[10] M.S. Nasir, G. Yang, I. Ayub, S. Wang, L. Wang, X. Wang, W. Yan, S. Peng, S. Ramakarishna, Recent development in graphitic carbon nitride based photocatalysis for hydrogen generation, Appl. Catal. B Environ. 257 (2019), 117855, https://doi.org/10.1016/j.apcatb.2019.117855.

[11] P. Kumar, D. Laishram, R.K. Sharma, A. Vinu, J. Hu, M.G. Kibria, Boosting photocatalytic activity using carbon nitride based 2D/2D van der Waals heterojunctions, Chem. Mater. 33 (2021) 9012–9092, https://doi.org/10.1021/acssuschemeng.2c00309.

[12] Q. Li, L. Zhang, J. Liu, J. Zhou, Y. Jiao, X. Xiao, C. Zhao, Y. Zhou, S. Ye, B. Jiang, Porous carbon nitride thin strip: precise carbon doping regulating delocalized π-electron induces elevated photocatalytic hydrogen evolution, Small 17 (2021), 2006622, https://doi.org/10.1002/smll.202006622.

[13] D. Jang, S. Choi, N.H. Kwon, K.Y. Jang, S. Lee, T.-W. Lee, S.-J. Hwang, H. Kim, J. Kim, S. Park, Water-assisted formation of amine-bridged carbon nitride: a structural insight into the photocatalytic performance for H₂ evolution under visible light, Appl. Catal. B Environ. 310 (2022), 121313, https://doi.org/10.1016/j.apcatb.2022.121313.

[14] J. Ding, Q. Tang, Y. Fu, Y. Zhang, J. Hu, T. Li, Q. Zhong, M. Fan, H.H. Kung, Core–shell covalently linked graphitic carbon

nitride–melamine–resorcinol–formaldehyde microsphere polymers for efficient photocatalytic CO₂ reduction to methanol, J. Am. Chem. Soc. 144 (2022) 9576–9585, https://doi.org/10.1021/jacs.1c13301.

[15] S. Lee, E.Y. Shin, D. Jang, S. Choi, H. Park, J. Kim, S. Park, Production of mesoporous carbon nitrides and their photocatalytic properties for degradation of organic pollutants, Bull. Kor. Chem. Soc. 43 (2022) 1124–1129, https://doi.org/10.1002/bkcs.12596.

[16] Y. Wang, L. Liu, T. Ma, Y. Zhang, H. Huang, 2D graphitic carbon nitride for energy conversion and storage, Adv. Funct. Mater. 31 (2021), 2102540, https://doi.org/10.1002/adfm.202102540.

[17] T. Huo, G. Ba, Q. Deng, F. Yu, G. Wang, H. Li, W. Hou, A dual strategy for synthesizing carbon/defect comodified polymeric carbon nitride porous nanotubes with boosted photocatalytic hydrogen evolution and synchronous contaminant degradation, Appl. Catal. B Environ. 287 (2021), 119995, https://doi.org/10.1016/j.apcatb.2021.119995.

[18] Y. Zhu, Y. Feng, S. Chen, M. Ding, J. Yao, Carbon nitride nanotube-based materials for energy and environmental applications: a review of recent progresses, J. Mater. Chem. 8 (2020) 25626–25648, https://doi.org/10.1039/D0TA08892G.

[19] D. Zhao, Y. Wang, C.-L. Dong, Y.-C. Huang, J. Chen, F. Xue, S. Shen, L. Guo, Boron-doped nitrogen-deficient carbon nitride-based Z-scheme heterostructures for photocatalytic overall water splitting, Nat. Energy 6 (2021) 388–397, https://doi.org/10.1038/s41560-021-00795-9.

[20] M. Talukdar, P. Deb, Recent progress in research on multifunctional graphitic carbon nitride: an emerging wonder material beyond catalyst, Carbon 192 (2022) 308–331, https://doi.org/10.1016/j.carbon.2022.02.060.

[21] Z. Zhao, Y. Long, Y. Chen, F. Zhang, J. Ma, Phosphorus doped carbon nitride with rich nitrogen vacancy to enhance the electrocatalytic activity for nitrogen reduction reaction, Chem. Eng. J. 430 (2022), 132682, https://doi.org/10.1016/j.cej.2021.132682.

[22] J. Oh, J.M. Lee, Y. Yoo, J. Kim, S.-J. Hwang, S. Park, New insight of the photocatalytic behaviors of graphitic carbon nitrides for hydrogen evolution and their associations with grain size, porosity, and photophysical properties, Appl. Catal. B Environ. 218 (2017) 349–358, https://doi.org/10.1016/j.apcatb.2017.06.067.

[23] Z. Zhou, Y. Zhang, Y. Shen, S. Liu, Y. Zhang, Molecular engineering of polymeric carbon nitride: advancing applications from photocatalysis to biosensing and more, Chem. Soc. Rev. 47 (2018) 2298–2321, https://doi.org/10.1039/C7CS00840F.

[24] H. Niu, W. Zhao, H. Lv, Y. Yang, Y. Cai, Accurate design of hollow/tubular porous g-C₃N₄ from melamine-cyanuric acid supramolecular prepared with mechanochemical method, Chem. Eng. J. 411 (2021), 128400, https://doi.org/10.1016/j.cej.2020.128400.

[25] O. Stroyuk, O. Raievska, D.R. Zahn, Graphitic carbon nitride nanotubes: a new material for emerging applications, RSC Adv. 10 (2020) 34059–34087, https://doi.org/10.1039/D0RA05580H.

[26] H. Kim, D. Jang, S. Choi, J. Kim, S. Park, Acid-activated carbon nitrides as photocatalysts for degrading organic pollutants under visible light, Chemosphere 273 (2021), 129731, https://doi.org/10.1016/j.chemosphere.2021.129731.

[27] M. Choi, S. Lee, D. Jang, S. Park, Production of Fe₃C/N-doped carbon hybrid and its electrocatalytic performance for oxygen evolution reactions, Carbon Lett. 32 (2022) 885–892.

[28] M. Thommes, K. Kaneko, A.V. Neimark, J.P. Olivier, F. Rodriguez-Reinoso, J. Rouquerol, K.S. Sing, Physisorption of gases, with special reference to the evaluation of surface area and pore size distribution (IUPAC Technical Report), Pure Appl. Chem. 87 (2015) 1051–1069, https://doi.org/10.1515/pac-2014-1117.

[29] X. Li, I.V. Sergeyev, F. Aussenac, A.F. Masters, T. Maschmeyer, J.M. Hook, Dynamic nuclear polarization NMR spectroscopy of polymeric carbon nitride photocatalysts: insights into structural defects and reactivity, Angew. Chem. 130 (2018) 6964–6968, https://doi.org/10.1002/ange.201802278.

[30] Y. Hu, Y. Shim, J. Oh, S. Park, S. Park, Y. Ishii, Synthesis of ¹³C-, ¹⁵N-labeled graphitic carbon nitrides and NMR-based evidence of hydrogen-bonding assisted two-dimensional assembly, Chem. Mater. 29 (2017) 5080–5089, https://doi.org/10.1021/acs.chemmater.7b00069.

[31] D.B. Nimbalkar, M. Stas, S.-S. Hou, S.-C. Ke, J.-J. Wu, Microscopic revelation of charge-trapping sites in polymeric carbon nitrides for enhanced photocatalytic activity by correlating with chemical and electronic structures, ACS Appl. Mater. Interfaces 11 (2019) 19087–19095, https://doi.org/10.1021/acsami.9b02494.

[32] H. Kim, D. Lim, N.H. Kwon, S. Son, S. Choi, J. Kim, S.-J. Hwang, S. Park, Dramatic change of morphological, photophysical, and photocatalytic H₂ evolution properties of C₃N₄ materials by the removal of carbon impurities, ACS Appl. Energy Mater. 3 (2020) 4812–4820, https://doi.org/10.1021/acsaem.0c00419.

[33] Y. Zhang, T. Mori, J. Ye, M. Antonietti, Phosphorus-doped carbon nitride solid: enhanced electrical conductivity and photocurrent generation, J. Am. Chem. Soc. 132 (2010) 6294–6295, https://doi.org/10.1021/ja101749y.

[34] Y.-j. Sun, J.-y. He, D. Zhang, X.-j. Wang, J. Zhao, R.-h. Liu, F.-t. Li, Simultaneous construction of dual-site phosphorus modified g-C₃N₄ and its synergistic mechanism for enhanced visible-light photocatalytic hydrogen evolution, Appl. Surf. Sci. 517 (2020), 146192, https://doi.org/10.1016/j.apsusc.2020.146192.

[35] H.-B. Fang, X.-H. Zhang, J. Wu, N. Li, Y.-Z. Zheng, X. Tao, Fragmented phosphorus-doped graphitic carbon nitride nanoflakes with broad sub-bandgap absorption for highly efficient visible-light photocatalytic hydrogen evolution, Appl. Catal. B Environ. 225 (2018) 397–405, https://doi.org/10.1016/j.apcatb.2017.11.080.

[36] Z. Liu, X. Zhang, Z. Jiang, H.-S. Chen, P. Yang, Phosphorus and sulphur co-doping of g-C₃N₄ nanotubes with tunable architectures for superior photocatalytic H₂ evolution, Int. J. Hydrogen Energy 44 (2019) 20042–20055, https://doi.org/10.1016/j.ijhydene.2019.06.037.

[37] H. Wang, B. Wang, Y. Bian, L. Dai, Enhancing photocatalytic activity of graphitic carbon nitride by codoping with P and C for efficient hydrogen generation, ACS Appl. Mater. Interfaces 9 (2017) 21730–21737, https://doi.org/10.1021/acsami.7b02445.

[38] N.N. Vu, C.C. Nguyen, S. Kaliaguine, T.O. Do, Synthesis of g-C₃N₄ nanosheets by using a highly condensed lamellar crystalline melamine–cyanuric acid supramolecular complex for enhanced solar hydrogen generation, ChemSusChem 12 (2019) 291–302, https://doi.org/10.1002/cssc.201802394.

[39] F. Jiang, R. Li, J. Cai, W. Xu, A. Cao, D. Chen, X. Zhang, C. Wang, C. Shu, Ultrasmall Pd/Au bimetallic nanocrystals embedded in hydrogen-bonded supramolecular structures: facile synthesis and catalytic activities in the reduction of 4-nitrophenol, J. Mater. Chem. 3 (2015) 19433–19438, https://doi.org/10.1039/C5TA02260F.

[40] A.M. Bakry, F.S. Awad, J.A. Bobb, A.A. Ibrahim, M.S. El-Shall, Melamine-based functionalized graphene oxide and zirconium phosphate for high performance removal of mercury and lead ions from water, RSC Adv. 10 (2020) 37883–37897, https://doi.org/10.1039/D0RA07546A.

[41] V. Sangeetha, N. Kanagathara, R. Sumathi, N. Sivakumar, G. Anbalagan, Spectral and thermal degradation of melamine cyanurate, J. Mater. 262094 (2013), https://doi.org/10.1155/2013/262094.

[42] P. Seggem, S.N. Chavan, S. Biswas, V.R. Jetti, Phosphate-based electrolyte and pristine graphite cathode for a high-voltage rechargeable dual-ion magnesium battery, ACS Appl. Energy Mater. 4 (2021) 5165–5174, https://doi.org/10.1021/acsaem.1c00709.

[43] Y. Zhang, K. Kou, T. Ji, Z. Huang, S. Zhang, S. Zhang, G. Wu, Preparation of ionic liquid-coated graphene nanosheets/PTFE nanocomposite for stretchable, flexible conductor via a pre-stretch processing, Nanomaterials 10 (2019) 40, https://doi.org/10.3390/nano10010040.

[44] J. Barrio, M. Shalom, Rational design of carbon nitride materials by supramolecular preorganization of monomers, ChemCatChem 10 (2018) 5573–5586, https://doi.org/10.1002/cctc.201801410.

[45] S. Zhao, J. Fang, Y. Wang, Y. Zhang, Y. Zhou, Poly (ionic liquid)-assisted synthesis of open-ended carbon nitride tube for efficient photocatalytic hydrogen evolution under visible-light irradiation, ACS Sustain. Chem. Eng. 7 (2019) 10095–10104, https://doi.org/10.1021/acssuschemeng.9b01544.

[46] C. Zhou, R. Shi, L. Shang, L.-Z. Wu, C.-H. Tung, T. Zhang, Template-free large-scale synthesis of g-C₃N₄ microtubes for enhanced visible light-driven photocatalytic H₂ production, Nano Res. 11 (2018) 3462–3468, https://doi.org/10.1007/s12274-018-2003-2.

[47] S. Zhao, Y. Liu, Y. Wang, J. Fang, Y. Qi, Y. Zhou, X. Bu, S. Zhuo, Carbon and phosphorus co-doped carbon nitride hollow tube for improved photocatalytic hydrogen evolution, J. Colloid Interface Sci. 616 (2022) 152–162, https://doi.org/10.1016/j.jcis.2022.02.057.

[48] S. Guo, Z. Deng, M. Li, B. Jiang, C. Tian, Q. Pan, H. Fu, Phosphorus-doped carbon nitride tubes with a layered micro-nanostructure for enhanced visible-light photocatalytic hydrogen evolution, Angew. Chem. (2016) 1830–1834, https://doi.org/10.1002/anie.201508505. Ed. 55.

[49] J. Ran, T.Y. Ma, G. Gao, X.-W. Du, S.Z. Qiao, Porous P-doped graphitic carbon nitride nanosheets for synergistically enhanced visible-light photocatalytic H₂ production, Energy Environ. Sci. 8 (2015) 3708–3717, https://doi.org/10.1039/C5EE02650D.

[50] S. Wang, F. He, X. Zhao, J. Zhang, Z. Ao, H. Wu, Y. Yin, L. Shi, X. Xu, C. Zhao, Phosphorous doped carbon nitride nanobelts for photodegradation of emerging contaminants and hydrogen evolution, Appl. Catal. B Environ. 257 (2019), 117931, https://doi.org/10.1016/j.apcatb.2019.117931.

[51] L. Jiang, X. Yuan, Y. Pan, J. Liang, G. Zeng, Z. Wu, H. Wang, Doping of graphitic carbon nitride for photocatalysis: a reveiw, Appl. Catal. B Environ. 217 (2017) 388–406, https://doi.org/10.1016/j.apcatb.2017.06.003.

[52] C.M. Lépori, N.M. Correa, J.J. Silber, R.D. Falcone, M. López-López, M.L. Moyá, Influence of the AOT counterion chemical structure on the generation of organized systems, Langmuir 36 (2020) 10785–10793, https://doi.org/10.1021/acs.langmuir.0c01575.

[53] Y. Liu, S. Zhao, Y. Wang, L. Xie, J. Fang, Y. Zhang, Y. Zhou, S. Zhuo, Controllable fabrication of 3D porous carbon nitride with ultra-thin nanosheets templated by ionic liquid for highly efficient water splitting, Int. J. Hydrogen Energy 46 (2021) 25004–25014, https://doi.org/10.1016/j.ijhydene.2021.05.018.

[54] Q. Su, X. Yao, W. Cheng, S. Zhang, Boron-doped melamine-derived carbon nitrides tailored by ionic liquids for catalytic conversion of CO₂ into cyclic carbonates, Green Chem. 19 (2017) 2957–2965, https://doi.org/10.1039/C7GC00279C.

[55] G. Zhang, A. Savateev, Y. Zhao, L. Li, M. Antonietti, Advancing the n → π* electron transition of carbon nitride nanotubes for H₂ photosynthesis, J. Mater. Chem. 5 (2017) 12723–12728, https://doi.org/10.1039/C7TA03777E.

[56] S. Guo, Z. Deng, M. Li, B. Jiang, C. Tian, Q. Pan, H. Fu, Phosphorus-doped carbon nitride tubes with a layered micro-nanostructure for enhanced visible-light photocatalytic hydrogen evolution, Angew. Chem. 128 (2016) 1862–1866, https://doi.org/10.1002/ange.201508505.

[57] C. Su, Y. Zhou, L. Zhang, X. Yu, S. Gao, X. Sun, C. Cheng, Q. Liu, J. Yang, Enhanced n → π* electron transition of porous P-doped g-C₃N₄ nanosheets for improved photocatalytic H₂ evolution performance, Ceram. Int. 46 (2020) 8444–8451, https://doi.org/10.1016/j.ceramint.2019.12.079.

[58] B. Choudhury, K.K. Paul, D. Sanyal, A. Hazarika, P. Giri, Evolution of nitrogen-related defects in graphitic carbon nitride nanosheets probed by positron annihilation and photoluminescence spectroscopy, J. Phys. Chem. C 122 (2018) 9209–9219, https://doi.org/10.1021/acs.jpcc.8b01388.

[59] H. Zhang, D. Zheng, Z. Cai, Z. Song, Y. Xu, R. Chen, C. Lin, L. Guo, Graphitic carbon nitride nanomaterials for multicolor light-emitting diodes and bioimaging, ACS

Appl. Nano Mater. 3 (2020) 6798–6805, https://doi.org/10.1021/acsanm.0c01197.

[60] D. Jang, H. Ahn, J. Oh, D. Lim, C.H. Kim, S. Choi, Y.H. Kim, J. Park, K.Y. Jang, R. J. Yoo, Production of Metal-free C, N alternating nanoplatelets and their in Vivo fluorescence imaging performance without labeling, Adv. Funct. Mater. 30 (2020), 2004800, https://doi.org/10.1002/adfm.202004800.

[61] H. Wahidah, J.W. Hong, Phosphorus-doped Pt nanowires as efficient catalysts for electrochemical hydrogen evolution and methanol oxidation reaction, Bull. Kor. Chem. Soc. 43 (2022) 1111–1117, https://doi.org/10.1002/bkcs.12594.